Fabrication of three dimensional split ring resonators by stress-driven assembly method

Che Chin Chen,[1] Chih Ting Hsiao,[2] Shulin Sun,[2,3] Kuang-Yu Yang,[4] Pin Chieh Wu,[2] Wei Ting Chen,[4] Yu Hsiang Tang,[1] Yuan-Fong Chau,[5] Eric Plum,[6] Guang-Yu Guo,[2,7] Nikolay I. Zheludev,[6] and Din Ping Tsai[1,2,4,8,*]

[1]*Instrument Technology Research Center, National Applied Research Laboratory, Hsinchu 30076, Taiwan*
[2]*Department of Physics, National Taiwan University, Taipei 10617, Taiwan*
[3]*National Center of Theoretical Sciences at Taipei, National Taiwan University, Taipei 10617, Taiwan*
[4]*Graduate Institute of Applied Physics, National Taiwan University, Taipei 10617, Taiwan*
[5]*Department of Electronic Engineering, Ching Yun University, Jung-Li 320, Taiwan*
[6]*Optoelectronics Research Centre and Centre for Photonic Metamaterials, University of Southampton, Southampton SO17 1BJ, UK*
[7]*Graduate Institute of Applied Physics, National Chengchi University, Taipei 11605, Taiwan*
[8]*Research Center for Applied Sciences, Academia Sinica, Taipei 115, Taiwan*
[*]*dptsai@phys.ntu.edu.tw*

Abstract: We demonstrate a self-assembly strategy for fabricating three dimensional (3D) metamaterials. This strategy represents the desired 3D curving prongs of the split ring resonators (SRRs) erected by metal stress force with appropriate thin film parameters. Transmittance spectra and field patterns corresponding to each resonance modes are calculated by finite element method (FEM). The eigen-modes of the SRRs can be excited by normal illumination with polarization state parallel to the erected SRRs, which are unlike for the cases of planar SRRs. This method opens a promising fabrication process for the application of tailored 3D SRRs.

References and links

1. J. B. Pendry, A. J. Holden, D. J. Robbins, and W. J. Stewart, "Magnetism from conductors and enhanced nonlinear," IEEE Trans. Microw. Theory Tech. **47**(11), 2075–2084 (1999).
2. J. Zhou, T. Koschny, M. Kafesaki, E. N. Economou, J. B. Pendry, and C. M. Soukoulis, "Saturation of the magnetic response of split-ring resonators at optical frequencies," Phys. Rev. Lett. **95**(22), 223902 (2005).
3. D. R. Smith, W. J. Padilla, D. C. Vier, S. C. Nemat-Nasser, and S. Schultz, "Composite medium with simultaneously negative permeability and permittivity," Phys. Rev. Lett. **84**(18), 4184–4187 (2000).
4. V. M. Shalaev, "Optical negative-index metamaterials," Nat. Photonics **1**(1), 41–48 (2007).
5. D. R. Smith, J. B. Pendry, and M. C. K. Wiltshire, "Metamaterials and negative refractive index," Science **305**(5685), 788–792 (2004).
6. C. Rockstuhl, T. Zentgraf, E. Pshenay-Severin, J. Petschulat, A. Chipouline, J. Kuhl, T. Pertsch, H. Giessen, and F. Lederer, "Optical magnetic responses in three-dimensional metamaterial of upright plasmonic meta-molecules," Opt. Express **15**, 8871–8883 (2007).
7. J. B. Pendry, "Negative refraction makes a perfect lens," Phys. Rev. Lett. **85**(18), 3966–3969 (2000).
8. N. Fang, H. Lee, C. Sun, and X. Zhang, "Sub-diffraction-limited optical imaging with a silver superlens," Science **308**(5721), 534–537 (2005).
9. R. Merlin, "Analytical solution of the almost-perfect-lens problem," Appl. Phys. Lett. **84**(8), 1290–1292 (2004).
10. J. B. Jackson and N. J. Halas, "Surface-enhanced Raman scattering on tunable plasmonic nanoparticle substrates," Proc. Nat. Acad. Sci. U.S.A. **101**(52), 17930–17935 (2004).
11. C. E. Talley, J. B. Jackson, C. Oubre, N. K. Grady, C. W. Hollars, S. M. Lane, T. R. Huser, P. Nordlander, and N. J. Halas, "Surface-enhanced Raman scattering from individual au nanoparticles and nanoparticle dimer substrates," Nano Lett. **5**(8), 1569–1574 (2005).
12. S. Nie and S. R. Emory, "Probing single molecules and single nanoparticles by surface-enhanced Raman scattering," Science **275**(5303), 1102–1106 (1997).
13. E. Plum, K. Tanaka, W. T. Chen, V. A. Fedotov, D. P. Tsai, and N. I. Zheludev, "A combinatorial approach to metamaterials discovery," J. Opt. **13**(5), 055102 (2011).
14. T. Kaelberer, V. A. Fedotov, N. Papasimakis, D. P. Tsai, and N. I. Zheludev, "Toroidal dipolar response in a metamaterial," Science **330**(6010), 1510–1512 (2010).
15. N. I. Zheludev, "Applied physics. The road ahead for metamaterials," Science **328**(5978), 582–583 (2010).

16. N. I. Zheludev, "A roadmap for metamaterials," Opt. Photon. News **22**(3), 30–35 (2011).
17. C. Rockstuhl, T. Zentgraf, E. Pshenay-Severin, J. Petschulat, A. Chipouline, J. Kuhl, T. Pertsch, H. Giessen, and F. Lederer, "The origin of magnetic polarizability in metamaterials at optical frequencies - an electrodynamic approach," Opt. Express **15**(14), 8871–8883 (2007).
18. N. Liu, H. Liu, S. Zhu, and H. Giessen, "Stereometamaterials," Nat. Photonics **3**(3), 157–162 (2009).
19. B. Lahiri, S. G. McMeekin, A. Z. Khokhar, R. M. De La Rue, and N. P. Johnson, "Magnetic response of split ring resonators (SRRs) at visible frequencies," Opt. Express **18**(3), 3210–3218 (2010).
20. S. Linden, C. Enkrich, M. Wegener, J. F. Zhou, T. Koschny, and C. M. Soukoulis, "Magnetic response of metamaterials at 100 terahertz," Science **306**(5700), 1351–1353 (2004).
21. R. A. Shelby, D. R. Smith, and S. Schultz, "Experimental verification of a negative index of refraction," Science **292**(5514), 77–79 (2001).
22. D. B. Burckel, J. R. Wendt, G. A. Ten Eyck, J. C. Ginn, A. R. Ellis, I. Brener, and M. B. Sinclair, "Micrometer-scale cubic unit cell 3D metamaterial layers," Adv. Mater. (Deerfield Beach Fla.) **22**(44), 5053–5057 (2010).
23. C. M. Soukoulis and M. Wegener, "Materials science. Optical metamaterials--more bulky and less lossy," Science **330**(6011), 1633–1634 (2010).
24. W. T. Chen, C. J. Chen, P. C. Wu, S. Sun, L. Zhou, G. Y. Guo, C. T. Hsiao, K. Y. Yang, N. I. Zheludev, and D. P. Tsai, "Optical magnetic response in three-dimensional metamaterial of upright plasmonic meta-molecules," Opt. Express **19**(13), 12837–12842 (2011).
25. K. Fan, A. C. Strikwerda, H. Tao, X. Zhang, and R. D. Averitt, "Stand-up magnetic metamaterials at terahertz frequencies," Opt. Express **19**(13), 12619–12627 (2011).
26. R. W. Hoffman, "Stresses in the thin films: the relevance of grain boundaries and impurities," Thin Solid Films **34**(2), 185–190 (1976).
27. O. G. Schmidt and K. Eberl, "Nanotechnology. Thin solid films roll up into nanotubes," Nature **410**(6825), 168 (2001).
28. Y. P. Ho, M. Wu, H.-Y. Lin, and W. Fang, "A robust and reliable stress-induced self-assembly supporting mechanism for optical devices," Microsyst. Technol. **11**, 214–220 (2005).
29. Y. V. Nastaushev, V. Y. Prinz, and S. N. Svitasheva, "A technique for fabricating Au/Ti micro- and nanotube," Nanotechnology **16**(6), 908–912 (2005).
30. J. W. Marvin, *Handbook of Optical Materials* (The CRC press, 2002).
31. L. Zhou and S. T. Chui, "Eigenmodes of metallic ring systems: A rigorous approach," Phys. Rev. B **74**(3), 035419 (2006).

1. Introduction

The metamaterials are the artificial structures which exhibiting unconventional engineered responses, such as artificial magnetism [1–3], negative index of refraction [4–6], sub-wavelength imaging [7, 8], field enhancement [9–13], and toroidal response [14]. Recently, metamaterials have attracted intense interests for a wide range of advanced applications [15, 16]. These tailored meta materials reveal their specific optical properties which are primarily dependent on the dimensions and configurations. The split ring resonators (SRRs) are the most common meta-molecule adopted in constructing the sub-wavelength structures [17, 18]. In particular, the behavior of a single SRR can be approximately considered as a LC circuit, in which the capacitor is contributed by the charges accumulating near the gap and the inductor is contributed by the surface current flowing inside the split ring [2, 19, 20]. The LC resonances can be excited by an incident light with electric field component parallel to the gap of the SRRs ($\vec{E}$ // $\hat{x}$) resulting in capacitance response or magnetic field component oscillating through the plane of the SRRs ($\vec{H}$ // $\hat{y}$) leading to inductance response, as shown in Fig. 1(c). In previous works, most of the SRR structures were focused on the planar types, i.e. the SRRs plane is lay on the substrate, due to the limited fabrication methods and the LC resonance mainly obtained through capacitance response. The induction response in planar SRRs can be performed only with the applied external light having an off-normal direction with respect to the SRRs plane, which thus lowers the coupling efficiency. So far, a few works were reported because of the challenge on fabrication processes for making three dimensional (3D) SRRs [21–25].

On the other hand, self assembly method utilizing residual thin film stress force had been demonstrated to form 3D devices, especially for curving structures [26–29]. The intrinsic stresses in thin films result from the lattice mismatch, grain boundaries, thermal expansion coefficient difference, impurities in the thin film, and deposition methods during film deposition. The 3D structure could be constructed by means of well arranging the material and dimensions of the deposited thin films.

In this paper, we demonstrate a relative simple method by adopting metal stress driven assembly strategy to fabricate the 3D SRRs. This strategy is simply combined with electron beam lithography (EBL) and reactive ion etching (RIE) processes, providing a promising way for the applications of 3D SRRs.

2. Fabrication procedures

A standard EBL (Raith 50, Raith GmbH) process is employed for pattering the 2D templates of the 3D SRRs with a total area of 200×200 µm^2 on fused silica substrate. Figure 1(a) represents the dimensions of a unit cell of the 2D templates with Al 15-nm-thick thickness. The arm length L and width W are 3 µm and 125 nm, respectively. The length (L_1) and width (L_2) of connection pad are 250 nm and 300 nm, respectively. Note that, the connection pad plays a role as a connection point between 3D SRRs and substrate, which is used to prevent the SRRs to be free standing structure after dry etching, as shown in Fig. 1(b). To avoid charging problem during e-beam exposure process, the Espacer (Kokusai Eisei Co., Showa Denso Group, Japan) is spin-coating above the PMMA-950K layer. After e-beam exposure, the sample is rinsed with de-ionized water to remove Espacer, and then developed in a solution of methyl isobutyl ketone (MIBK) and isopropyl alcohol (IPA) of MIBK:IPA = 1:3 for 75 seconds, and then in IPA for 25 second.
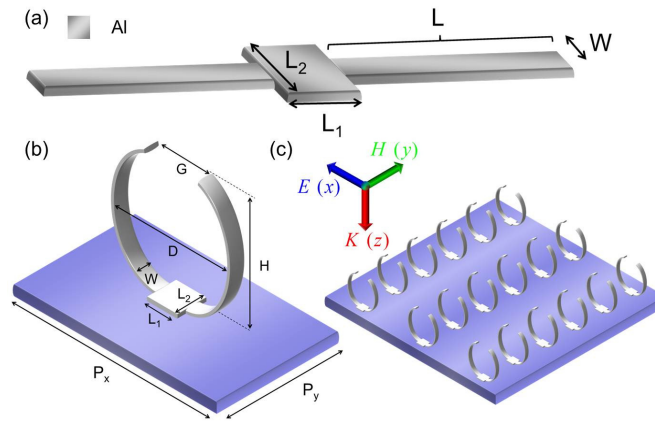

Fig. 1. The schematic diagram with the feature sizes of 3D SRRs before (a) and after (b) released from the substrate by dry etching method. The parameters of our designed SRRs are L_1 = 250 nm, L_2 = 300 nm, W = 125 nm, H = 2 µm, D = 2 µm, G = 600 nm, P_x = 8 µm and P_y = 3 µm, respectively. (c) The fabricated sample is illuminated by an x-polarized light at normal incidence.

The aluminum film is deposited on the patterned resist by thermal evaporation (DMC 500, Dah Young Vacuum Technical Co., Ltd). The thickness of deposited aluminum film is monitored by ULVAC MDEL CRTM-6000 Quartz Crystal Deposition Controller and the deposition rate is about 0.5 Å/sec with stable pressure of 5×10^{-5} Torr. Subsequent to the lift-off process, the sample with 2D templates are transferred into the dry etching machine (Plasmalab System 100-ICP 380, Oxford Instruments Plasma Technology) to etch the fused silica which is underneath the arms and then release the arms from substrate. As the arms of 2D templates released from the substrate, the intrinsic stress force pulls up the arms leading to 3D SRRs simultaneously, as shown in Fig. 1(c).

3. Results and discussions

The bending results in our experiment depend on the arm dimensions and film thickness. Therefore, in the first stage, we pattern 2D arms with different arm width W and length L to clarify the influence of geometric factors corresponding to the same thickness of metallic film. The 2D arms pattern is defined and etched as shown in Fig. 2(a). Note that, to obtain continuous Al film, the thickness was firstly deposited with 15 nm for all 2D patterns in this

paper. The left and right column corresponding to the case $W = 125$ nm and $W = 250$ nm, respectively. The arm length L varies from 3 µm to 9 µm in a step of 2 µm. The bending results shown in Fig. 2(b) manifest that, with the same L, the radii of curvature are increased with increased W. In contrast, with the same W, the curving structures exhibit similar radii of curvature.

Based on the above-mentioned phenomena, we thus turn our attention to film thickness effects on the bending. In the Fig. 3, the bending effect is studied by varying the thickness of thin film. The radii of curvature are strongly dependent on the film thickness. The 2D unit cell is designed with $L = 2$ µm and $L = 3$ µm, respectively, corresponding to the same width $W = 125$ nm. After C_4F_8 dry etching process, the arms are released from the substrate. Figures 3(a) and 3(d) show the arm length $L = 2$µm and $L = 3$µm with the same 8-nm-thick Al film, respectively. The thickness is estimated by comparing the etching rate between fused silica and Al. We then apply Ar plasma to gently mill the Al for obtaining the thinner Al film. Figures 3(b) and 3(e) show the SRRs with estimated film thickness about 5 nm for the case of gap $G = 500$ nm, $L = 2$ µm and $G = 400$ nm, $L = 3$µm, respectively. In the case of 4-nm-thick Al film, the smaller G about 250 nm and 50 nm corresponding to $L = 2$ µm and $L = 3$ µm is observed, as shown in Figs. 3(c) and 3(f). Moreover, regarding the thermal expansion of metal films, we perform the live images of SEM as well, as shown in Media 1, presenting that the gap of SRR could be tuned by thermal expansion in response to temperature changes from electron beam scanning. This result demonstrates that the fabricated stress-driven SRRs may be an excellent candidate for developing the temperature controlled reconfigurable metamaterial.
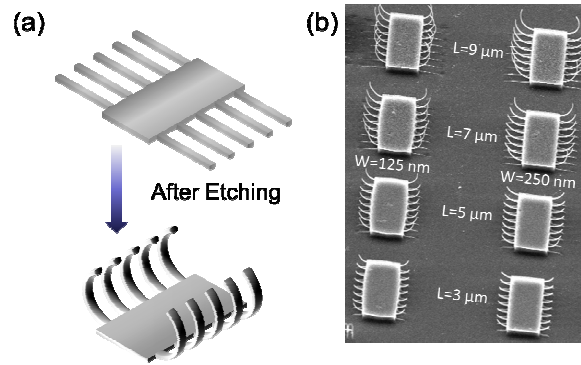

Fig. 2. (a) The schematic diagrams of test arms before and after dry etching process. (b) The oblique view of SEM micrographs with tilting angle of 40þfor the test arms. The pattern is designed for four kinds of arm lengths with two different arm widths, respectively.

To illustrate the electromagnetic resonance modes of the fabricated erected SRRs, we employed COMSOL Multiphysics to calculate the transmittance spectra and field patterns of different resonance modes by solving the 3D Maxwell equations on the basis of finite element method. The dimensions of a simulated unit cell are shown in Fig. 1(b) and with the same geometric parameters of the fabricated sample. To simulate a SRRs array, periodic conditions are used at the boundaries of the unit cell. The optical parameters of aluminum in the near and middle infrared regime were taken from the optics handbook [30] and refractive index of the substrate is set as 1.4584.
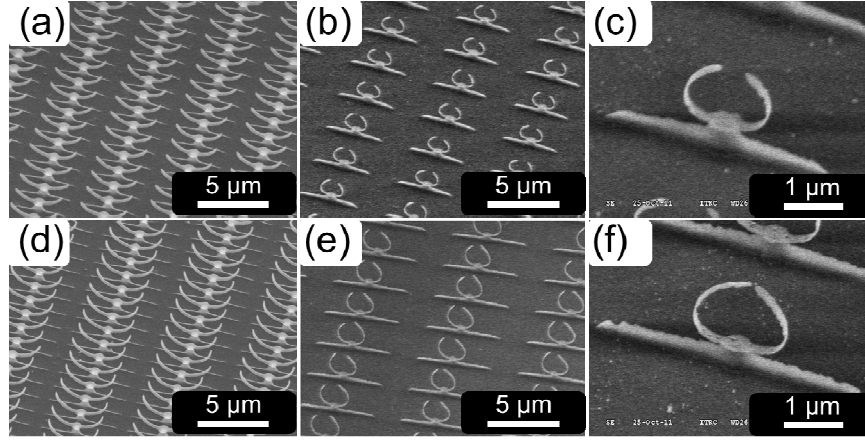
Fig. 3. The oblique view of SEM micrographs with tilting angle of 40 degree for the 3D SRRs. (a), (b) and (c) show SRRs with the same arm length of 2μm but with different Al film thickness, respectively. The metal thickness (a) = (d) = 8 nm, (b) = (e) = 5 nm and (c) = (f) = 4 nm, respectively. Figures (d), (e) and (f) are the SRRs with arm length of 3 μm. Notice that the bar-shapes on the substrate represent the residual fused silica material underneath the metal film, resulting from the shadow effect of etching process.

The transmittance spectra of the SRRs array are shown in Fig. 4(a). The electric field of the normal incident waves ($\vec{k} \parallel \hat{z}$) is polarized along x and y directions, respectively. The transmittance spectrum is almost flat for the y-polarized case because neither electric nor magnetic resonance modes can be excited. Conversely, three resonance modes appear at about 20.8 THz, 39.0 THz, and 62.8 THz for x-polarized case. Considering the gap width can be manipulated by many experimental methods (for example electron beam excitation or adjusting the environment temperatures), the electromagnetic response of the SRRs can be controlled correspondingly. To demonstrate these reconfigurable properties, we simulated SRRs arrays with different gap width: G = 250 nm, 600 nm, 1200 nm and 2000 nm. In four cases, the total arm length of SRR is kept same but the parameters D and H are different. To illustrate the spectra change clearly, the transmittance spectra of mode 1 are shown in Fig. 4(b). Obviously "mode 1" shifts towards high frequency region while the gap width is increased. It can be qualitatively understood in the picture of equivalent LC circuit model. The total length of SRR kept same means that the effective inductance almost does not change. But the capacitances of the equivalent circuit will definitely decrease while the gap width becomes larger. Considering that the resonance frequency is proportional to $1/\sqrt{L_{eff}C_{eff}}$, the blue-shift of the resonance modes with increasing gap width is a natural result.

The magnetic field patterns of the three resonance modes are shown in Figs. 4(c)-(e). The intensity is normalized to the magnitude of incident magnetic fields. For the single SRR in ring geometry, its eigen-states have been carefully studied by Zhou et al. [31]. Different eigen-states of SRRs can be excited under several polarization cases (that is $\vec{k} \parallel \hat{z}$, $\vec{E} \parallel \hat{x}$; $\vec{k} \parallel \hat{z}$, $\vec{E} \parallel \hat{x}$; $\vec{k} \parallel \hat{y}$, $\vec{E} \parallel \hat{z}$; $\vec{k} \parallel \hat{x}$, $\vec{E} \parallel \hat{z}$). Here the magnetic field enhancement effect of "mode 1" and "mode 3" is larger than 10, and the "mode 2" has only 5 times enhancement. To understand it, we need to analysis the induced current distributions of the three modes which can be demonstrated by simulation just like the cases shown in Figs. 4(f)-(h). For "mode 1", the magnetic responses of the induced currents are parallel, so the magnetic strength is very strong and the transmission dip is the deepest. For "mode 2", the magnetic response of the induced currents will be destructive inside the ring and constructive outside the ring. And electric response along x direction are introduced by the air gap. For "mode 3", it also have electric and magnetic response simultaneously. Finally, we need to emphasize that

when the metal film gets very thin, its response to incident EM waves drops significantly, which may diminish the resonance of a SRR.
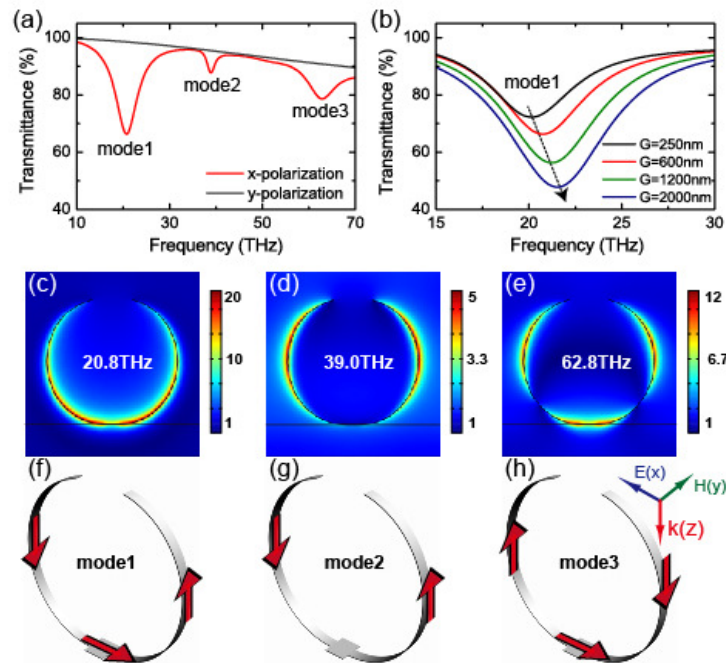

Fig. 4. The simulation transmittance spectra of the SRR arrays with (a) the same geometric and (b) the same total length but different gap widths (G = 250 nm, 600 nm, 1200 nm, and 2000 nm) based on the unit cell shown in Fig. 1(b). In (a), there exists three transmission dips at about 20.8 THz, 39.0 THz and 62.8 THz for x-polarization case. The magnetic field patterns and the induced current distribution (red arrow) of three resonance modes in the case of G = 600 nm are shown in (c)-(e) and (f)-(h), respectively. Here both of the spectra and field patterns are normalized to the incident waves.

4. Summary

In conclusion, we successfully fabricate 3D SRRs by a simple stress-driven assembly method. The tailored 3D SRRs can be constructed through precise arrangement of film parameters of the 2D templates. The radii of curvature of erected arms are decreased with decreasing arm width or film thickness under the same arm length. In addition, we have also observed the tunable characteristic depending on the temperature changes of our SRRs. By means of this strategy, we actually fabricate a new kind of 3D, upright, and tunable metamaterials. Transmittance spectra and magnetic field patterns of the fabricated 3D SRRs are calculated by FEM simulation which demonstrates that both electric and magnetic resonance modes can be excited with x-polarized normal incident wave. A blue-shift of the resonance modes with increasing gap width is investigated in the case of reconfigurable application.